INTERNATIONAL JOURNAL FOR NUMERICAL METHODS IN FLUIDS
Int. J. Numer. Meth. Fluids **29**: 865–876 (1999)

THE COMPUTATION OF TURBULENT FLOW THROUGH STATIONARY AND ROTATING U-BENDS WITH RIB-ROUGHENED SURFACES

H. IACOVIDES*

Department of Mechanical Engineering, UMIST, Manchester M60 1QD, UK

SUMMARY

This study focuses on the numerical computation of turbulent flow through stationary and rotating U-ducts of square cross-section, with rib-roughened inner and outer walls along the straight sections. Square-sectioned ribs, normal to the flow direction are employed in a staggered arrangement. The rib height-to-diameter ratio is 0.1 and the rib pitch-to-rib height ratio is 10. The bend curvature ratio (R_c/D) is 0.65 and the flow Reynolds number is 100000. The duct rotates about an axis parallel to that of curvature, at a rotation number ($Ro \equiv \pm 0.2$). The preliminary computations presented suggest that grid requirements can be significantly reduced, through a combination of body fitted grids and high-order convective discretisation schemes in all transport equations. The presence of regions of flow separation, necessitates the use of low *Re* second-moment closures. Flows through negatively rotating U-bends are found to be especially challenging to turbulence models. Copyright © 1999 John Wiley & Sons, Ltd.

KEY WORDS: U-bend; orthogonal rotation; rib-roughness; second-moment closures

1. INTRODUCTION

Flow and heat transfer through U-bends of strong curvature is of direct relevance to the internal cooling of gas turbine blades. In modern gas turbines, relatively cool air extracted from compressor stages of the engine is circulated through internal cooling passages inside the turbine rotor blades, in order to maintain the operating temperature of the blades at safe levels. The flow development and consequently, the heat transfer characteristics inside these cooling passages are affected by the presence of sharp U-bends, the rotation of the blades and the presence of heat transfer enhancing ribs.

In three-dimensional flows through either curved or rotating passages, both the Coriolis and the curvature force induce strong secondary motions (see Moon [1] and Chang *et al.* [2]). As earlier work has shown [3–5], the presence of secondary motion in flows through curved passages, necessitates the integration of the mean flow equations across the viscous wall sublayer, making it inappropriate to use the widely employed wall function approach. Moreover, as work in the author's group revealed [3,6], the introduction of second-moment closures, instead of using effective viscosity models, further improves flow and heat transfer predictions, for both curved and rotating flows. For flows in smooth U-bends of strong curvature, strong enough to cause flow separation, the author's earlier work [7], provided

---

* Correspondence to: Department of Mechanical Engineering, UMIST, Manchester M60 1QD, UK.

CCC 0271–2091/99/070865–12$17.50

Received December 1997
Revised March 1998

evidence that it also becomes necessary to employ high-order schemes for the discretisation of convective transport, in all transport equations for both mean and turbulent flow variables. The recent emergence of detailed LDA measurements [8] for flow through tight U-bends, stationary and rotating, motivated further numerical investigations [9]. They revealed that one of the most important features of these flows, namely the flow separation along the inner wall of the U-bend, is better captured when the use of second-moment closures is extended across the viscous wall sublayer.

The experimental work of the UMIST [10] group has recently produced detailed LDA measurements for flows through ribbed U-bends under both stationary and rotating conditions, as shown in Figure 1. The numerical simulation of such flows is expected to require the use of fine three-dimensional grids. In this contribution, an attempt is being reported to reduce grid requirements by employing non-orthogonal body fitted grids and also high-order discretisation schemes (a bounded form of the QUICK scheme). A further objective of this work is to carry out an initial assessment of the performance of effective viscosity and second-moment closures in the prediction of such flows.

While both two- and three-dimensional computations of flow and heat through ribbed passages can be found in the scientific literature (e.g. Taylor *et al.* [11], Liou *et al.* [12]), this study contains more detailed comparisons with extensive local flow data.

2. FLOW EQUATIONS

All equations are expressed here in Cartesian tensor notation, for a rotating frame of reference.

2.1. Mean motion

Continuity

$$\frac{\partial}{\partial x_i}(\rho U_i) = 0.$$

Momentum transport

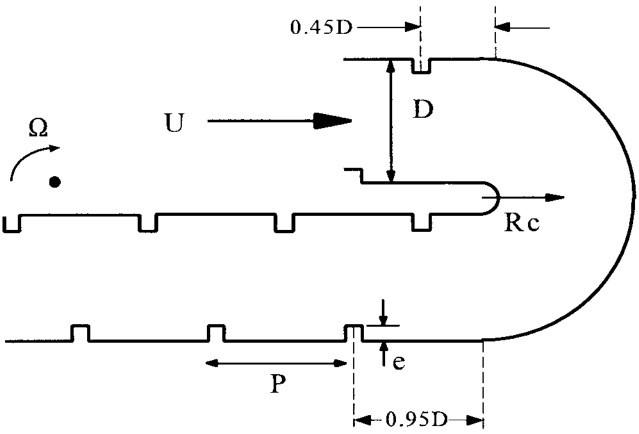

Figure 1. Flow geometry.

$$\frac{\partial}{\partial x_j}(\rho U_i U_j) = -\frac{\partial P}{\partial x_i} + \frac{\partial}{\partial x_j}\left[\mu\left(\frac{\partial U_i}{\partial x_j} + \frac{\partial U_j}{\partial x_i}\right) - \rho\overline{u_i u_j}\right] - 2\rho\epsilon_{ijp}\Omega_p U_j - \rho[\Omega_j X_j \Omega_i - \Omega_j X_i \Omega_j].$$

2.2. Turbulent flow equations

The earlier studies, discussed in Section 1, suggest that a low Reynolds number model of turbulence needs to be employed across the near-wall regions, and that the use of second-moment closures is also desirable. In order to reconcile these requirements with the need for grid economy, two zonal models have been selected; the high *Re* version of the $k-\epsilon$ matched to a low *Re* one-equation model of k transport and a simple version of the stress transport model, arising from an ASM closure also employed in previous U-bend computations [9], in which across the near-wall regions, the dissipation rate of turbulence is obtained from the near-wall distance.

2.2.1. Effective viscosity model (EVM).

$$\rho\overline{u_i u_j} = \frac{2}{3}k\delta_{ij} - \mu_t\left(\frac{\partial U_i}{\partial x_j} + \frac{\partial U_j}{\partial x_i}\right) \quad \text{and} \quad \mu_t = \rho c_\mu \frac{k^2}{\epsilon},$$

$$\frac{\partial}{\partial x_j}(\rho U_j k) = \frac{\partial}{\partial x_j}\left[(\mu + \mu_t)\frac{\partial k}{\partial x_j}\right] + P_k - \rho\epsilon, \quad P_k = -\rho\overline{u_i u_j}\left(\frac{\partial U_i}{\partial x_j}\right),$$

$$\frac{\partial}{\partial x_j}(\rho U_j \epsilon) = \frac{\partial}{\partial x_j}\left[\left(\mu + \frac{\mu_t}{\sigma_\epsilon}\right)\frac{\partial \epsilon}{\partial x_j}\right] + c_{\epsilon 1}\frac{\epsilon}{k}P_k - \rho c_{\epsilon 2}\frac{\epsilon^2}{k}.$$

Across the near-wall regions (Wolfshtein [13]):

$$\epsilon = \frac{k^{3/2}}{\ell_\epsilon} \quad \text{and} \quad \mu_t = \rho c_\mu \ell_\mu \sqrt{k}.$$

The length scales ℓ_ϵ and ℓ_μ are obtained from the near-wall distance Y, according to:

$$\ell_\epsilon = 2.55Y[1 - \exp(-0.263y^*)] \quad \text{and} \quad \ell_\mu = 2.55Y[1 - \exp(-0.016y^*)],$$

where $y^* \equiv Yk^{1/2}/v$ is the dimensionless wall distance.

2.2.2. Differential stress model.

$$\frac{\partial}{\partial x_k}(\rho U_k \overline{u_i u_j}) = \frac{\partial}{\partial x_k}\left[(\mu + \mu_t)\frac{\partial \overline{u_i u_j}}{\partial x_k}\right] + P_{ij} - \rho\epsilon_{ij} + \phi_{ij} - \left[H_{ij} - \frac{1}{3}H_{kk}\delta_{ij}\right] + J_{ij},$$

$$P_{ij} = -\left[\overline{u_i u_k}\frac{\partial U_j}{\partial x_k} + \overline{u_j u_k}\frac{\partial U_i}{\partial x_k}\right] - 2\Omega_p(\epsilon_{ipq}\overline{u_q u_j} + \epsilon_{ijpq}\overline{u_q u_i}),$$

$$\epsilon_{ij} = \frac{2}{3}(1 - f_\epsilon)\epsilon\delta_{ij} + f_\epsilon\frac{\overline{u_i u_k}}{k}\epsilon,$$

$$\phi_{ij} = -c_1\frac{\epsilon}{k}\left(\overline{u_i u_j} - \frac{2}{3}k\delta_{ij}\right) - c_2\left(P_{ij} - \frac{2}{3}P_k\delta_{ij}\right) + f_w(\phi^w_{ij1} + \phi^w_{ij2}).$$

The conventional wall reflection terms are used, which rely on the wall distance x_n and the unit vector normal to the wall n.

$$\phi^w_{ij,1} = c^w_1\frac{\epsilon}{k}\left(\overline{u_k u_m}n_k n_m\delta_{ij} - \frac{3}{2}\overline{u_k u_i}n_k n_j - \frac{3}{2}\overline{u_k u_j}n_k n_i\right)\left\{\frac{k^{1.5}}{\epsilon c_\ell x_\mathrm{n}}\right\},$$

$$\phi^{w}_{ij,2} = c^{w}_{2}\frac{\epsilon}{k}\left(\phi_{km2}n_k n_m\delta_{ij} - \frac{3}{2}\phi_{ik2}n_k n_j - \frac{3}{2}\phi_{ik2}n_k n_i\right)\left\{\frac{k^{1.5}}{\epsilon c_\ell x_{\mathrm{n}}}\right\},$$

$$\phi_{ij2} = -c_2\left(P_{ij} - \frac{2}{3}P_k\delta_{ij}\right).$$

The low *Re* terms H_{ij} and J_{ij} are defined as:

$$H_{ij} = f_H\frac{v}{k}\left(\overline{u_i u_\ell}\frac{\partial\sqrt{k}}{\partial x_\ell}\frac{\partial\sqrt{k}}{\partial x_j} + \overline{u_j u_\ell}\frac{\partial\sqrt{k}}{\partial x_\ell}\frac{\partial\sqrt{k}}{\partial x_i}\right) \qquad J_{ij} = f_J k\left(\frac{\partial U_i}{\partial x_j} + \frac{\partial U_j}{\partial x_i}\right).$$

The damping functions that appear in the above terms have the following expressions:

$$f_\epsilon = \exp(-y^*/3) \qquad f_w = [1 - \exp(-0.12y^*)][1 + \exp(-0.03y^*)]$$

$$f_J = 0.06\exp(-y^*/3) \qquad f_H = (10.2 + 7.5y^*)\exp(-y^*/20).$$

The dissipation rate equation is identical to that used in the EVM model. In the near-wall regions, the dissipation rate c, is also obtained from a prescribed length scale ℓ_ϵ, defined as:

$$\ell_\epsilon = 2.55Y[1 - \exp(-0.236y^*)].$$

The constants that appear in the turbulence equations have the following values.

$c_{\epsilon 1}$	$c_{\epsilon 2}$	c_μ	σ_ϵ	c_1	c_2	c^w_1	c^w_2	c_ℓ
1.44	1.92	0.09	1.30	1.8	0.6	0.5	0.3	2.55

3. NUMERICAL ASPECTS

A three-dimensional non-orthogonal finite volume solver, STREAM, was employed, developed at UMIST. A collocated grid is employed with mass flux modification to prevent pressure chequer boarding. In the case of the DSM model, use of the apparent viscosity concept prevents numerical oscillations arising from the explicit presence of the Reynolds stress gradients in the momentum transport equations.

For the discretisation of convective transport, earlier attempts to compute flows through U-bends of curvature strong enough to cause flow separation [7] revealed that it was necessary to employ a high-order discretisation scheme for all transport equations. The scheme previously employed, a bounded form of the QUICK [14] scheme proposed by Zhu and Leschziner [15] called LODA, while effective in minimising numerical errors, led to problems of numerical stability. For this reason, an alternative bounding mechanism has been developed during the course of this study and employed in these computations.

Within the control volume approach, the problem of convective discretisation amounts to that of finding the value of the discretised variable, Ψ, at the control volume faces, as indicated in Figure 2. In the QUICK scheme, a quadratic internodal variation is used. Two of the three nodal values needed to determine the assumed parabolic variation, are placed on the upwind side and one on the downwind side of each face. In order to prevent unphysical oscillations along each direction, the use of QUICK is limited to cells where the variation of the discretised variable is monotonic. The criteria adopted arise from the examination of the quadratic

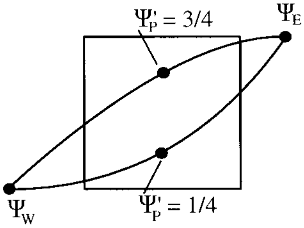

Figure 2. One-dimensional stencil.

variation of Ψ across each cell that can be obtained from its nodal value at the cell centre and those at the two neighbouring cells. As shown in Figure 2, the QUICK scheme is used only when the gradient of this parabolic distribution of the variable between the two neighbouring nodes does not change sign. For a uniform grid distribution along each direction, this requirement results in using QUICK only when the normalised value of nodal variable, $\Psi'_P \equiv (\Psi_P - \Psi_W)/(\Psi_E - \Psi_W)$ is between 1/4 and 3/4. For Ψ'_P between 1/4 and 0 and 3/4 and 1, weighted averages of the QUICK and UPWIND values of Ψ are used at the west and east cell faces, while for Ψ'_P less than 0 or greater than 1, the pure upwind values are employed.

Thus, for each direction the scheme is summarised as follows:

$$\Psi'_P \equiv (\Psi_P - \Psi_W)/(\Psi_E - \Psi_W)$$

$1/4 < \Psi'_P < 3/4$	QUICK vales can be used for east and west faces
$0 < \Psi'_P < 1/4$	$4\Psi'_P$ of QUICK value $+ (1 - 4\Psi'_P)$ of UPWIND value
$3/4 < \Psi'_P < 1$	$4(1 - \Psi'_P)$ of QUICK value $+ (4\Psi'_P - 3)$ of UPWIND value
$\Psi'_P < 0$ or $\Psi'_P > 1$	UPWIND values must be used for east and west faces

To ensure consistency at each face, the lower-order value of the two neighbouring cells is adopted.

4. CASES EXAMINED

Three cases have been computed, all of identical flow geometry, which as shown in Figure 1, is that of a tight U-bend of square cross-section, with square ribs, normal to the flow direction, along the inner and outer walls of the straight upstream and downstream sections. The bend curvature ratio R_c/D, has a value of 0.65. The rib height-to-diameter ratio, e/D is 0.1 and the rib pitch-to-rib height ratio is 10. The flow Reynolds number is 100000. In the first case, the U-bend is stationary, while for the other two, the bend rotates orthogonally about an axis parallel to that of curvature, either positively, where the pressure (trailing) side coincides with the outer side of the bend, or negatively. In both rotating cases, the rotation number ($Ro \equiv \Omega D/U_B$) is 0.2. This mode of rotation was chosen because the flow remains symmetric about the geometric plane of symmetry. Data for comparison has been produced by Iacovides *et al.* [10].

A body fitted grid has been employed as shown in Figure 3, consisting of 38 nodes across the duct, 15 from the symmetry plane to the top (smooth) wall and 147 planes in the streamwise direction. This type of grid has been chosen because it allows a more efficient resolution of the near-wall regions. In all cases, preliminary computations were carried out for repeating flow over a single rib interval in order to generate entry flow conditions. These

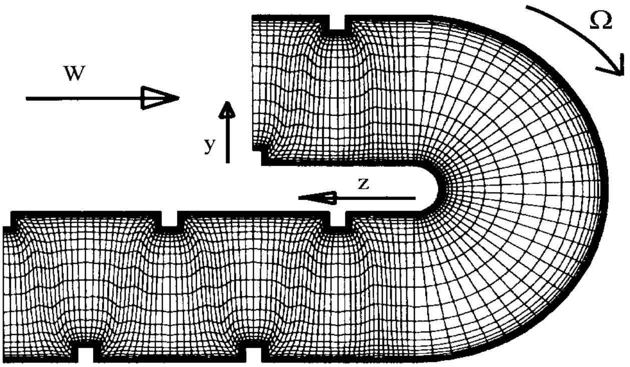

Figure 3. Grid employed for U-bend flow.

repeating flow computations were also used to assess the suitability of the grid employed. Two grids were employed for the repeating flow computations; a 38 × 32 × 15 mesh having the same grid density as the U-bend mesh of Figure 4, and a 76 × 64 × 30 mesh, which is twice as dense in each direction. The resulting EVM comparisons, shown in Figure 5, reveal that the mean flow computations produced by these two grids are identical and in close agreement with the LDA measurements. This provides clear evidence supporting the use of body fitted grids in the computation of flows through ribbed ducts.

5. RESULTS AND DISCUSSION

For the stationary duct, the computed and measured mean flow developments along the symmetry plane are first compared through the vector plots of Figure 6. The measurements show that at the bend entry, there is a small region of flow separation along the outer wall, due to the presence of a rib half a diameter upstream. At the exit, a larger separation bubble is formed along the inner wall, which extends beyond the first downstream rib, 0.45*D* after the exit. The measurements also show that along the outer wall, as the high momentum fluid from

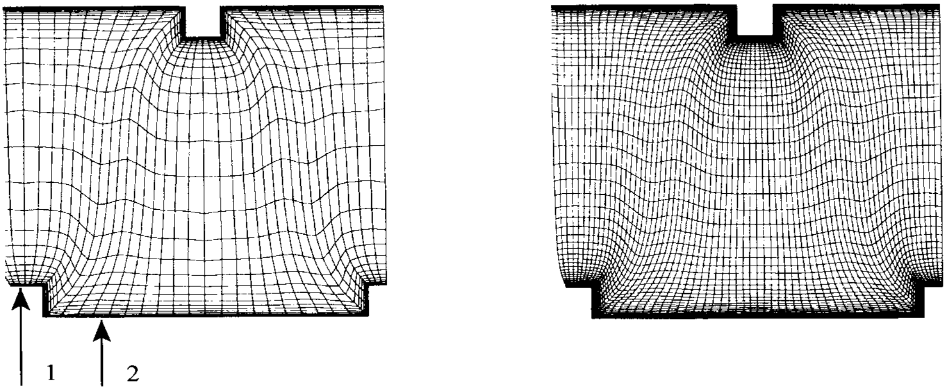

(a) (b)

Figure 4. Grids used for repeating flow computations; (a) 38 × 32 × 15, (b) 76 × 64 × 30.

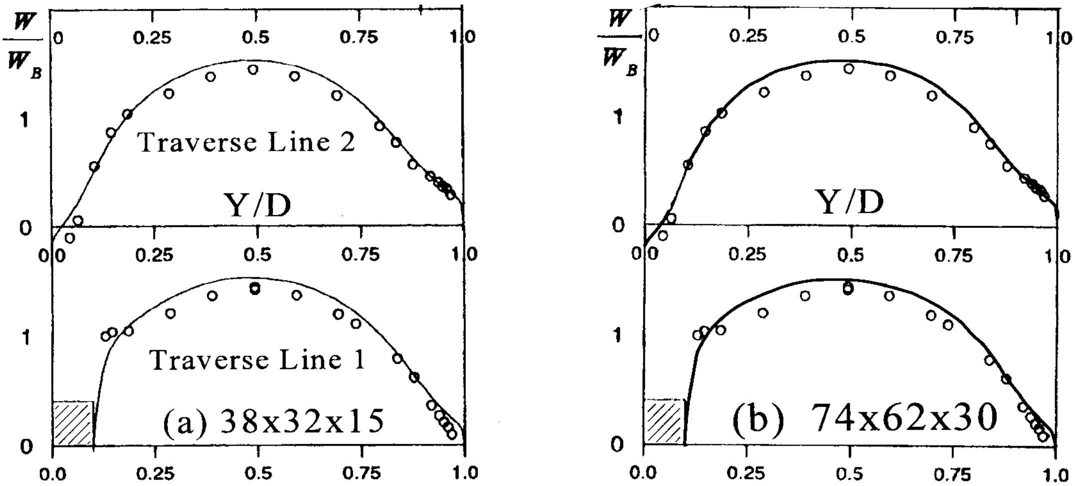

Figure 5. Grid comparisons of repeating flow computations for EVM model; —, EVM computations; ○ ○ ○ ○, experimental data [10].

the bend exit meets the first downstream rib, 0.95*D* from the exit, a large separation bubble is formed over the subsequent rib interval. The corresponding computations reveal that both models reproduce well the overall flow features, but the details of flow separation and subsequent reattachment are more faithfully captured by the DSM computations. These findings are also confirmed by the more detailed profile comparisons of Figure 7. They show

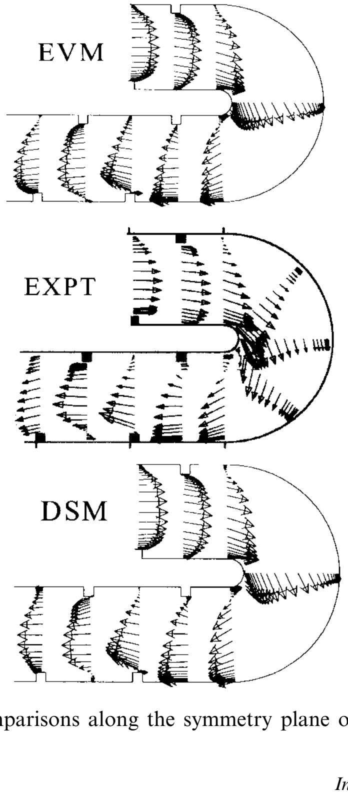

Figure 6. Vector comparisons along the symmetry plane of a stationary U-bend.

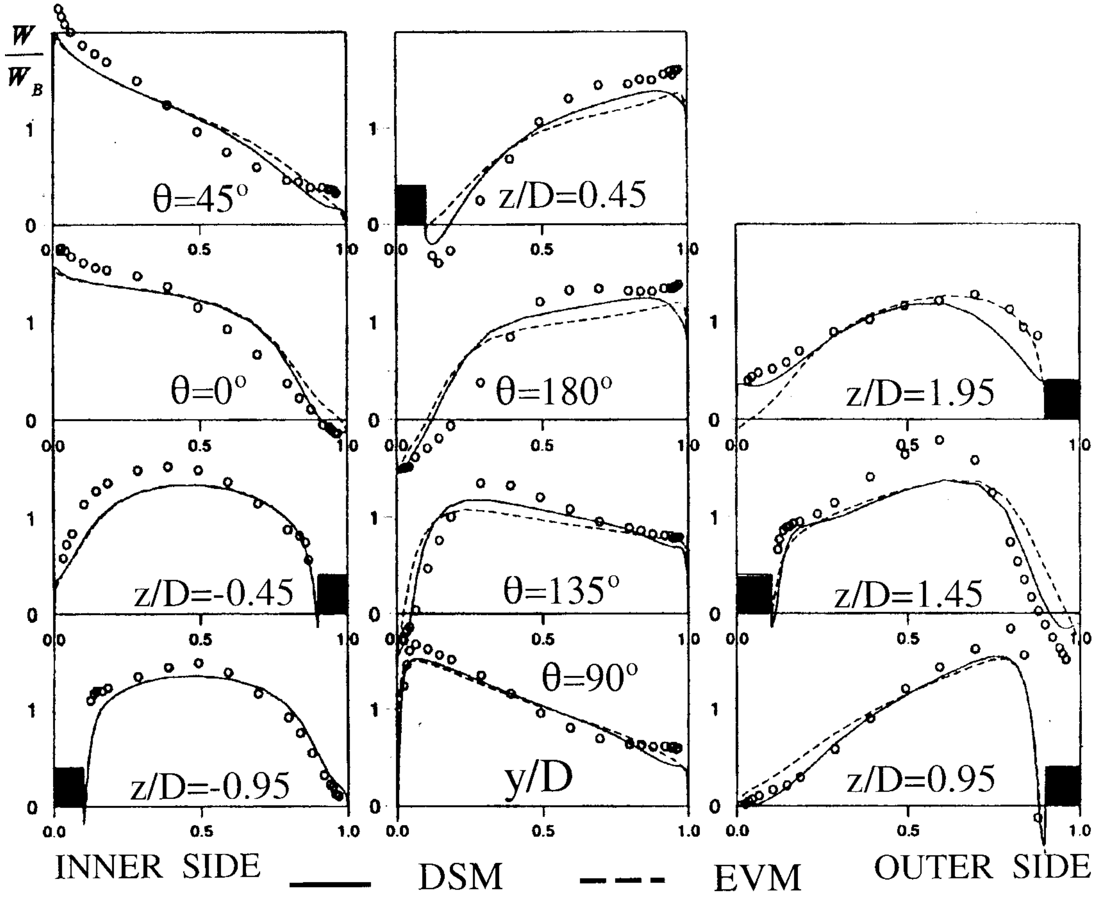

Figure 7. Comparisons of streamwise velocity profiles along the symmetry plane of a stationary U-bend; ○ ○ ○ ○, experimental data [10]; —, DSM; ----, EVM.

that rib-induced, as well as curvature-induced, flow separations are better predicted through the use of low *Re* second-moment closures. As well as demonstrating the superiority of low *Re* second-moment closures, the comparisons also indicate that the numerical approach that followed resulted in numerically clean mean flow predictions for this complex U-bend flow. Comparisons for the cross-duct velocity component, not shown here, lead to observations consistent with those for the streamwise velocity component.

Figures 8 and 9 present mean flow comparisons for the case of positive rotation, in the form of vector plots and profiles of the streamwise velocity respectively. In the upstream section, positive rotation transfers the high momentum fluid to the outer (pressure) side of the duct. This feature is well captured by both models. At the bend entry, the measurements show that the positive rotation prevents flow separation along the outer wall. Both models however, predict that along the outer wall, the flow remains separated for the first 45° of the bend. Agreement between predictions and measurements improves from the 90° plane, especially for the DSM model. On the whole, as also found in earlier studies, for smooth U-bends [9], flow through the positively rotating U-bend is well-predicted by the models employed.

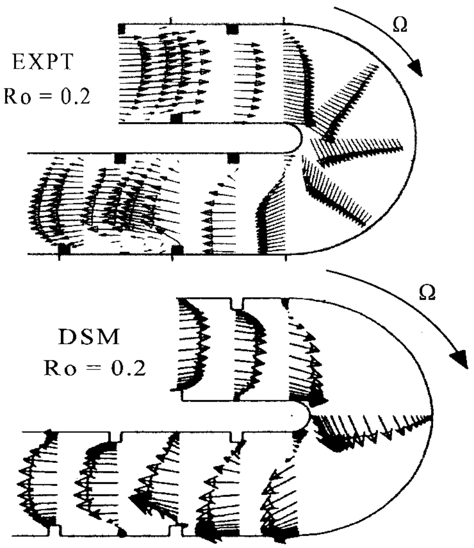

Figure 8. Vector field comparisons along the symmetry plane positively rotating U-bend.

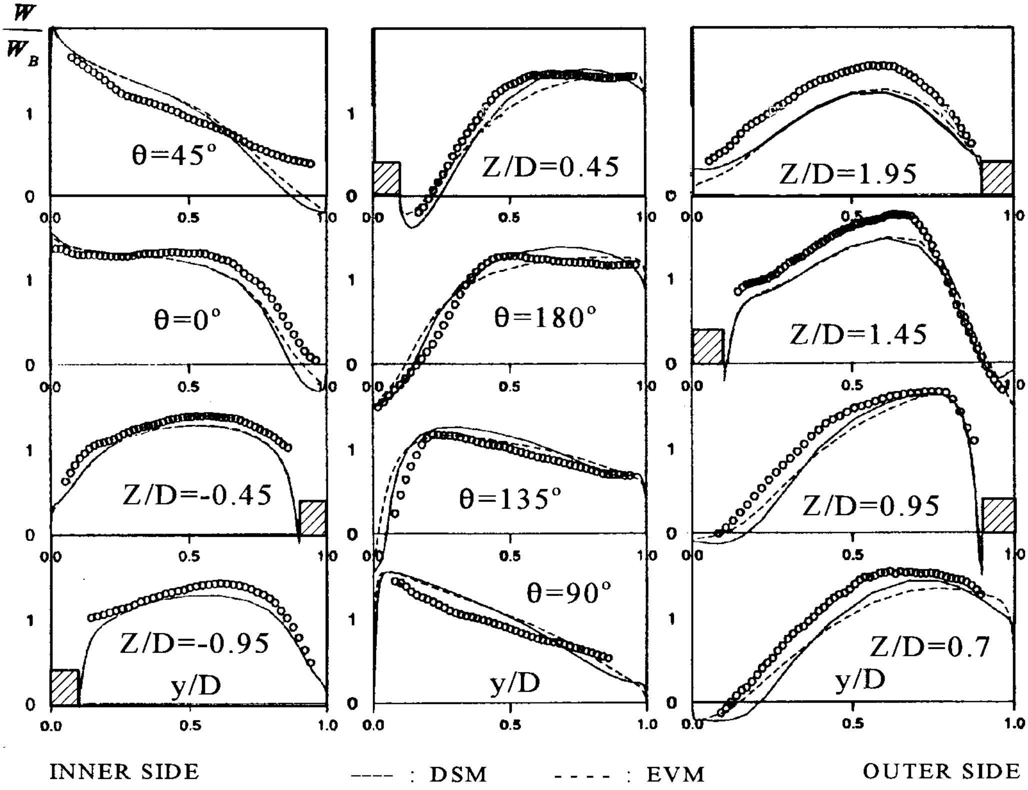

Figure 9. Comparisons of streamwise velocity profiles along the symmetry plane of a positively rotating U-bend; ○ ○ ○ ○, experimental data [10]; – – –, DSM; ----, EVM.

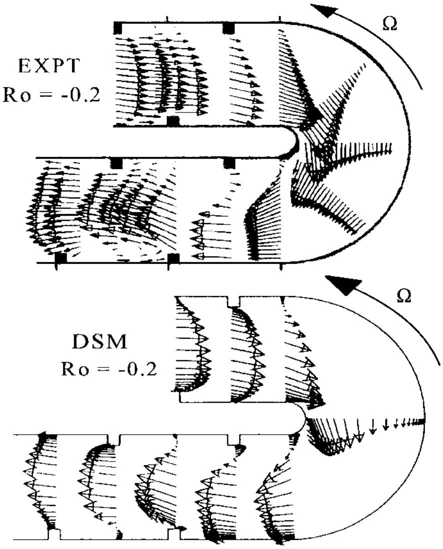

Figure 10. Vector field comparisons along the symmetry plane of negatively rotating U-bend.

The corresponding comparisons of Figures 10 and 11, for negative rotation, indicate that when the Coriolis force opposes that of curvature, the predictive performance of the models tested starts to deteriorate. While the inlet conditions do faithfully reproduce those of the experimental study [10], noticeable differences between the computed and measured behaviour appear even before the bend entry. Deviations from the measured behaviour persist throughout the bend and in the immediate downstream region, especially for the EVM model. Nevertheless, the main flow features are still returned by both models. It thus appears, that the combined effects of rib roughness and strong curvature are well-captured by the simple low *Re* DSM closure employed in this study, while the EVM model exhibits weaknesses in regions of flow separations, which have also been noted in earlier studies through smooth U-bends. The addition of negative rotation does, however, further complicate the turbulence field and agreement between computations and measurements becomes qualitative rather than quantitative. A closer examination of the predicted turbulence fields is now in progress, in order to identify the causes.

6. CONCLUDING REMARKS

In this study a set of computations of turbulent flows through stationary and rotating rib-roughened U-bends have been carried out in order to explore both numerical and turbulence modelling issues related to such numerical predictions.

On the numerical side, it has been shown that the use of body fitted grids and high-order schemes for the discretisation of the convective transport of all flow variables, grid requirements can be significantly reduced leading to reliable mean flow predictions, even for the relatively coarse mesh employed[1].

---

[1] More recent flow computations for the same U-bend, using four times as many grid nodes also confirm this conclusion.

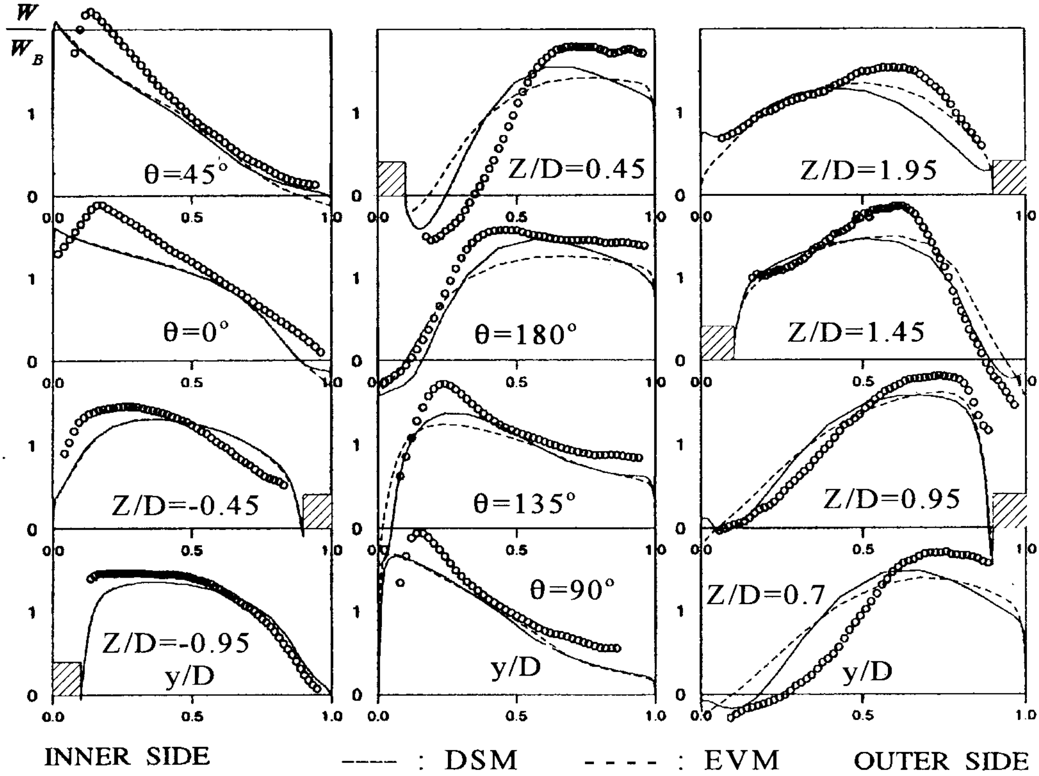

Figure 11. Comparisons of streamwise velocity profiles along the symmetry plane of a negatively rotating U-bend; – – –, DSM; ----, EVM.

As far as turbulence modelling is concerned, the comparisons suggest that a low *Re* second-moment closure becomes necessary in order to reliably predict the regions of flow separation, induced by strong curvature and the presence of ribs. The second-moment closure used in this study, was however, unable to fully account for the effects of negative rotation, where the Coriolis and curvature forces oppose each other. Further, finer mesh computations are now in progress, in which the predicted turbulence fields would be closely examined.

ACKNOWLEDGMENTS

The author wishes to express his gratitude to his colleague Professor B.E. Launder, for his support and encouragement. Support for this work has been provided by Rolls Royce plc and DRA Pyestock. The helpful input of Mr J. Coupland, of Rolls Royce plc is gratefully acknowledged. Thanks are also due to Dr Y.-M. Yuan at UMIST for making available the experimental data in digital form.

REFERENCES

1. I.M. Moon, 'Effects of Coriolis force on the turbulent boundary layer in rotating fluid machines', *Report No. 74*, MIT Gas Turbine Laboratory, 1964.
2. S.M. Chang, J.A.C. Humphrey, R.W. Johnson and B.E. Launder, 'Turbulent momentum and heat transport in flow through a 180° bend of square cross-section', *Proc. 4th Symp on Turbulent Shear Flows*, Karlsruhe, 1983, pp. 620–625.

3. Y.-D. Choi, H. Iacovides and B.E. Launder, ‘Numerical computation of turbulent flow in a square-sectioned 180° bend’, *ASME J. Fluids Eng.*, **111**, 59–68 (1989).
4. J.Y. Xia and C. Taylor, ‘The prediction of turbulent flow and heat transfer in a tight square cross-sectioned 180° bend’, *Proc. 8th Int. Conf. on Numerical Methods in Laminar and Turbulent Flows*, Swansea, 1993.
5. D.L. Besserman and S. Tanrikut, ‘Comparison of heat transfer measurements with computations for turbulent flow around a 180° bend’, *ASME Paper 91-GT-2*, *Int. Gas Turbine and Aero Congress*, Orlando FL, 1991.
6. T. Bo, H. Iacovides and B.E. Launder, ‘Developing buoyancy modified turbulent flow in ducts rotating in orthogonal mode’, *ASME J. Turbomach.*, **117**, 474–484 (1995).
7. T. Bo, H. Iacovides and B.E. Launder, ‘Convective discretisation schemes for the turbulence transport equations in flow predictions through sharp U-bends’, *Int. J. Numer. Methods Heat Fluid Flow*, **5**, 33–48 (1995).
8. S.C. Cheah, H. Iacovides, D.C. Jackson, H. Ji and B.E. Launder, ‘LDA investigation of the flow development through rotating U-ducts’, *ASME J. Turbomach.*, **118**, 590–596 (1996).
9. H. Iacovides, B.E. Launder and H.-Y. Li, ‘The computation of flow development through stationary and rotating U-bends of strong curvature’, *Int. J. Heat Fluid Flow*, **17**, 22–23 (1995).
10. H. Iacovides, D.C. Jackson, H. Ji, G. Kelemenis, B.E. Launder and K. Nikas, ‘LDA study of flow development through an orthogonally rotating U-Bend of strong curvature and rib-roughened walls’, *Paper No. ASME-96-GT-476*, *Int. Gas Turbine and Aero Congress*, Birmingham, UK, June 1996.
11. C. Taylor, J.Y. Xia, J.O. Medwel and W.D. Morris, ‘Numerical simulation of three-dimensional turbulent flow and heat transfer within a multiribbed cylindrical duct’, *Paper No. ASME 91-GT-8*, *Int. Gas Turbine and Aero Congress*, Orlando, FL, USA, 1991.
12. T.-M. Liou, J.-J. Hwang and S.-H. Chen, ‘Simulation and measurement of enhanced turbulent heat transfer in a channel with periodic ribs on one principal wall’, *Int. J. Heat Mass Transf.*, **36**, 507–517 (1993).
13. M. Wolfstein, ‘The velocity and temperature distribution in one-dimensional flow with turbulence augmentation and pressure gradient’, *Int. J. Heat Mass Transf.*, **12**, 301 (1969).
14. B.P. Leonard, ‘A stable and accurate convective modelling procedure based on quadratic interpolation’, *Comput. Methods Appl. Mech. Eng.*, **19**, 59–98 (1979).
15. H. Zhu and M.A. Leschziner, ‘A local oscillation-damping algorithm for higher-order convection schemes’, *Comput. Methods Appl. Mech. Eng.*, **67**, 355 (1988).